Geometry and kinetics determine the microstructure in arrested coalescence of Pickering emulsion droplets

SCHOLARONE™
Manuscripts

Journal Name

Geometry and kinetics determine the microstructure in arrested coalescence of Pickering emulsion droplets

Zhaoyu Xie[a], Christopher J. Burke[a], Badel Mbanga[a], Patrick T. Spicer [b], and Timothy J. Atherton[a,c]

Arrested coalescence occurs in Pickering emulsions where colloidal particles adsorbed on the surface of the droplets become crowded and inhibit both relaxation of the droplet shape and further coalescence. The resulting droplets have a nonuniform distribution of curvature and, depending on the initial coverage, may incorporate a region with negative Gaussian curvature around the neck that bridges the two droplets. Here, we resolve the relative influence of the curvature and the kinetic process of arrest on the microstructure of the final state. In the quasistatic case, defects are induced and distributed to screen the Gaussian curvature. Conversely, if the rate of area change per particle exceeds the diffusion constant of the particles, the evolving surface induces local solidification reminiscent of jamming fronts observed in other colloidal systems. In this regime, the final structure is shown to be strongly affected by the compressive history just prior to arrest, which can be predicted from the extrinsic geometry of the sequence of surfaces in contrast to the intrinsic geometry that governs the static regime.

1 Introduction

Pickering emulsions incorporate micro- or nano-scale colloidal particles that adsorb onto the fluid-fluid interface of the constituent droplets. The presence of these particles stabilizes the emulsion against phase separation by inhibiting processes like *coalescence* where droplets combine[1–3]. Arrested coalescence occurs when two initial droplets with coverage fraction ϕ_i above some critical value ϕ_c coalesce. As the doublet relaxes toward a spherical shape due to surface tension, the particles become crowded and inhibit further relaxation, producing a nonspherical droplet with a rigid interfacial shell that prevents further coalescence of additional droplets. The point of arrest can be predicted from ϕ_i and the relative size of the two droplets: once ϕ for the combined droplet would exceed $\phi_c = \pi/\sqrt{12} \approx 0.9$, the value of hexagonal packing in 2D, the coalescence will be arrested. If ϕ_i is increased, coalescence is arrested at an earlier point. Arrest can also be achieved by other offsetting rheological resistance such as internal viscoelastic fluids[4].

In addition to increased stability, arrested coalescence is a straightforward method for sculpting non-spherical droplets.

While other studies[1–3] have shown how to control the shape of the arrested droplets, the particle microstructure of the arrested structures has not been studied. The purpose of this paper is, therefore, to predict the microstructure from the final shape and to disentangle the static and kinetic influences.

Where relaxation of the doublet proceeds sufficiently slowly that the particles are in quasistatic equilibrium with the host shape, the problem may be approached from the view of spherical crystallography[5], for which Pickering emulsion droplets—*colloidosomes*—have proven an ideal model system[6]. On curved surfaces, dislocations in the crystal—particles with a contact number c_i other than 6—are required to accomodate the curvature. Moreover, because the shape is a closed surface, the structure is subject to the topological constraint that $\sum_i q_i = 6\chi$, where $q_i = c_i - 6$ is the defect charge and χ the Euler characteristic of the surface is 2. Dislocations beyond those required by topology occur if the cost of forming a dislocation is favorable relative to distorting the lattice[7–15] and form grain boundaries or *scars* to help screen the Gaussian curvature[6,9]. Nonuniform curvature leads to localization of the defects[15–18].

Kinetic effects remain unexamined in the assembly of colloidosomes before, but have received extensive attention in other related systems. The response of solid amorphous materials under deformation is described by the shear-transformation-zone (STZ) theory[19–21], whereby localized clusters of molecules (the eponymous STZs) undergo irreversible non-affine rearrangements in re-

[a] *Department of Physics and Astronomy, Tufts University, 574 Boston Avenue, Medford, Massachusetts 02155, USA*

[b] *Complex Fluids Group, School of Chemical Engineering, UNSW Sydney, Sydney, Australia*
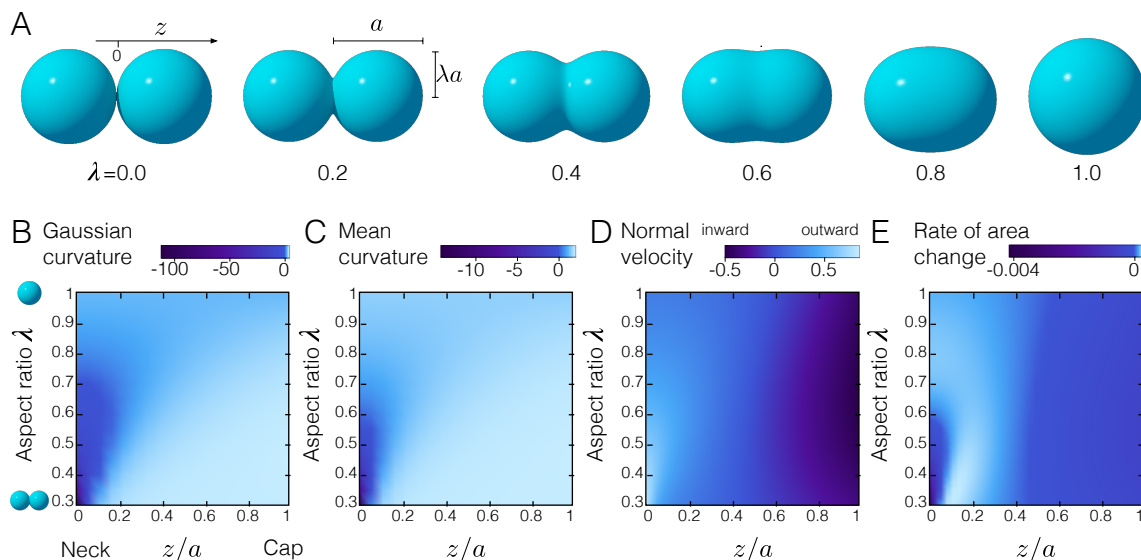
[c] *Email: timothy.atherton@tufts.edu*

Fig. 1 Ansatz fluid-fluid interface shape. (A) Simulation of different stages of coalescence parametrized by λ. (B-D) Differential geometry of the family of surfaces: (B) Gaussian curvature; (C) Mean curvature; (D) Normal velocity and (E) local rate of area change γ. All quantities are plotted as a function of λ (at fixed volume) and distance z/a along the rotational symmetry axis of the surface.

sponse to applied shear stresses. The STZ provides a wealth of theoretical tools for characterizing such systems. A second source of inspiration are studies that probe solidification in complex fluids: Under impact, for example, dense suspensions of colloidal particles rapidly solidify from the point of impact with a propagating dynamic jamming front[22]. Similar processes have been observed with other kinds of forcing such as shear and extension[23–25]. More generally, arrested coalescence falls into the interesting class of nonequilibrium systems that develop a "memory" of their evolution[26].

Arrested coalescence has some common features with these other systems, but, importantly, the deformations involved are spatially varying due to the curvature and not driven by external influences. To develop our description, the rest of the paper is structured as follows: in Section 2 we analyze the differential geometry of the shapes that occur in arrested coalescence and develop a framework for analyzing the kinetic contribution. We then separate the influence of geometry and kinetics on the microstructure by comparing static packings produced with a fixed shape in section 3 and kinetic packings produced as the shape relaxes towards the final spherical ground state in section 4. Prospects for exploiting these effects are discussion in the concluding Section 5.

2   Theory

In this section, we analyze the influence of the evolving shape on the structure adopted by N spherical particles of radius r embedded upon it. A central assumption of this work is that the evolution of the surface is predetermined and not modified by the presence of the particles, whose centers of mass are constrained to the surface but are free to move around it according to some dynamics to be specified. This assumption agrees with experimental observations of Pickering emulsions[1,2,27].

An analytical *ansatz* to describe the shape evolution of a pair of spherical droplets as they relax following coalescence was proposed by Garabedian *et al.*[28]. After initial contact, the surface is described by the level set,

$$\frac{a^2\lambda^2(x^2+y^2)+a^2z^2}{(x^2+y^2+z^2)^2} = 1, \qquad (1)$$

where a is the half length of long axis and the aspect ratio $\lambda \in [0,1]$ controls the extent of coalescence as shown in Fig. 1A. The value $\lambda = 0$ corresponds to the two droplets just touching each other and $\lambda = 1$ represents the final state as one spherical droplet. The center is located at the origin and the z axis is the axis of rotational symmetry. The value a is chosen for each λ to hold the total volume of the surface constant. Experimentally observed arrested structures in[1,4] are well described by Eq. (1), justifying the assumption of specified shape evolution.

To understand the influence of the evolving shape on arrested particle structures, we now study the differential geometry of the family of surfaces described by Eq. (1). The distribution of dislocations in static packings is known to be controlled by the distribution of Gaussian curvature, which acts like a nonuniform background defect charge distribution in addition to the discrete defect charges for the elastic term in free energy[14]. We therefore display in Fig. 1B the Gaussian curvature along the axis of rotation z as a function of λ where a is also varied to maintain a fixed volume of $\pi/3$.

During the initial stages of relaxation, i.e. $\lambda \lesssim 0.7$, the neck of the doublet creates a region where the Gaussian curvature K is negative while at the ends of the droplet the curvature approaches a constant value because here the surface is almost spherical. In this regime, the neck region should induce negative defects, which requires additional compensating positive defects to meet the overall topological constraint. As λ increases, the profile $K(z)$

becomes smoothed over time until it approaches a uniform constant value for the spherical final state. Beyond $\lambda = 0.7$, therefore, we expect to see the defect distribution skewed towards the cap where the K is largest, reducing to a uniform distribution as $\lambda \to 1$. These predictions for the static case will be tested in Section 3.

We now turn to kinetic effects. The process driving arrest is the shrinking of surface area, quantified by $\dot{A}$ the rate of change of the area of the surface. This quantity plays a similar role to the strain rate for media under deformation, though we emphasize that here strain is more complicated as it is spatially varying. We shall also assume some other process that relaxes the configurations toward their equilibrium state. Here, the relaxing process will be diffusion with an in-plane diffusion coefficient D and associated timescale τ_d defined through $2r = \sqrt{2D\tau_d}$.

Since $\dot{A}$ and D have the same dimensions, a natural dimensionless parameter that quantifies the importance of kinetics emerges,

$$\Gamma = \frac{\dot{A}}{ND} = \frac{1}{N}\frac{dA}{dt}\frac{\tau_d}{2r^2} = \frac{1}{2r^2 N}\frac{\tau_d}{\tau_r}\frac{dA}{dT}, \tag{2}$$

where τ_r is the time of full relaxation which may be used to nondimensionalize time $T = t/\tau_r$; this quantity measures the rate of change of area per particle relative to the diffusion constant. The ratio,

$$\theta = \tau_d/\tau_r \tag{3}$$

also emerges as a measure of the relative influence of diffusion and relaxation and is in practice the independent variable that will be varied to construct our ensemble of simulations. For the surfaces described by Eq. (1), the quantity dA/dT is almost linearly related to λ for all but small values of $\lambda < 0.1$ (Fig. S1) where the *ansatz* is a poor approximation to the experiment[1], and so we shall not investigate arrest in this regime.

We shall also construct a local version of (2),

$$\gamma = \frac{\dot{a}}{nD}, \tag{4}$$

where a is the area of some region of interest Ω on the surface and n is the number of particles in that region. The quantity γ captures the local rate of expansion or contraction per particle measured relative to their diffusion, and therefore predicts regions where the particles may become crowded. Note that (4) captures only one form of deformation, scaling, imparted on the particles by the evolving surface. As shown in Fig. S2, the local deformation in the neck also involves stretching in the azimuthal direction.

The quantity $\dot{A}$ can be computed from more fundamental objects as follows. Consider a one-parameter family of surfaces $\mathbf{X}(\lambda)$—Eq. (1) is an example—that describes the shape evolution of the surface. The rate of change of area can then be written,

$$\dot{A} = \int \nabla \cdot \mathbf{N}\left(\frac{d\mathbf{X}}{d\lambda}\cdot\mathbf{N}\right)\frac{d\lambda}{dt}dA, \tag{5}$$

where $\mathbf{N}$ is the local outward surface normal and the integral is over the surface. The first factor is the divergence of the normal and can be rewritten in terms of the mean curvature H, while the second factor in (5) is the normal component of the velocity (with
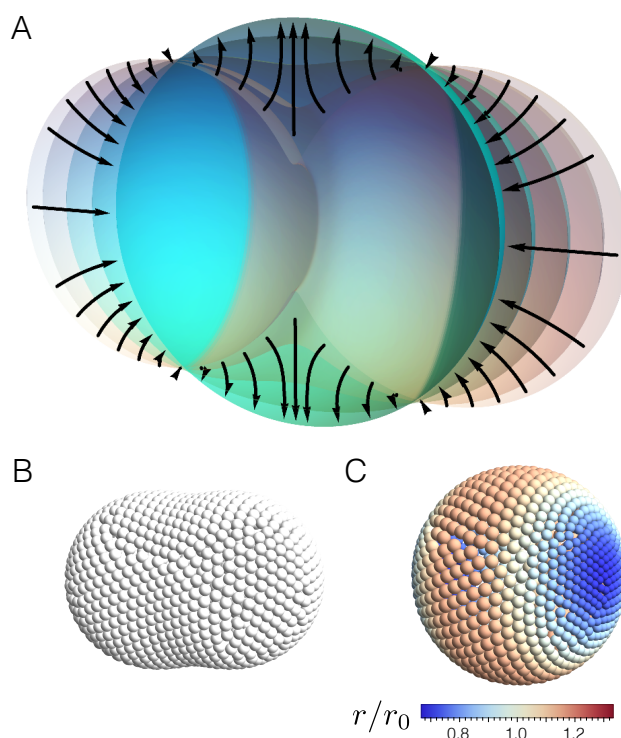

r/r_0 0.8   1.0   1.2

Fig. 2 (A) **Trajectories followed by particles** at different starting locations that move only under constraint forces as the surface evolves. (B) An arrested configuration at $\lambda = 0.6$ with equal size particles of radius r_0 can be conformally mapped onto (C) a configuration with different sized particles on final spherical state $\lambda = 1$ by transporting the particles along the normal trajectories shown in A and scaling them according to a local r/r_0.

sign measured with respect to the outward normal) as the surface evolves according to $\lambda(t)$. The integrand of (6) is identified as $\dot{a}$ and hence an explicit formula for γ can be constructed,

$$\gamma = \frac{1}{nD}\frac{d\lambda}{dt}\int_\Omega 2H\left(\frac{d\mathbf{X}}{d\lambda}\cdot\mathbf{N}\right)dA \tag{6}$$

where the integral is taken over a region of interest on the surface containing n particles.

The three factors in (6) each contain different information: the first, $\frac{d\lambda}{dt}$ supplies the overall time dependence and is strictly positive. The second, H, can be directly calculated from instantaneous configurations of the surface. It is famously related to the capillary pressure difference across the surface Δp through the Young-Laplace equation,

$$\Delta p = 2\sigma H \tag{7}$$

where σ is the surface tension and therefore measures the local generalized force acting to minimize the surface area. The final factor in (6) $\frac{d\mathbf{X}}{d\lambda}\cdot\mathbf{N}$ captures the velocity induced by evolution of the surface and necessarily incorporates the effect of the volume constraint.

We note that (6) reveals an elegant distinction: the microstructure of the static packings is determined by the Gaussian curvature, an *intrinsic* quantity, while the role of kinetics is determined

by *extrinsic* quantities—those that depend on how the surface is embedded—such as the mean curvature. Previous literature has focussed on the role played by the Gaussian curvature on packing[7–15,29] as well as crystallization and nucleation[30–33], while little attention has been paid to the role of extrinsic geometry.

We now examine the ramifications of (6) for the kinetics of arrest on the present surface (1). First, the time dependence $\lambda(t)$ is chosen such that the radius of the neck scales $\propto t^{1/2}$. This form was proposed for the inertial regime where Reynolds number is large by Eggers *et al.*[34] and confirmed experimentally[35,36] to hold in the early stages of coalescence. We use this power law for the whole process for simplicity.

Next, the mean curvature H is displayed in Fig. 1C and like the Gaussian curvature exhibits a negative region at the neck for early stages of the relaxation. The normal velocity is shown for different λ in Fig. 1D and the product of these terms in Fig. 1E.

To help interpret these quantities, consider a single free particle at rest on the initial surface that moves only subject to constraint forces as the surface evolves and neglect the inertia of the particles which is assumed to be damped by the surrounding fluid. The constraint forces must act in the direction locally normal to the surface and hence the particles follow trajectories such as those in Fig. 2A shown for different starting positions around the doublet.

In some locations, for example the caps, the trajectories in Fig. 2A are strictly convergent and the product $H\left(\frac{d\mathbf{X}}{d\lambda}\cdot\mathbf{N}\right)$ is negative for all λ, indicating that particles here tend to be compressed as the doublet relaxes. By contrast, in the neck a region of strong compression exists for $\lambda < 0.6$ which becomes expansive as the surface approaches the final spherical state. These features arise because the discriminant γ arises *both* from the sign of the mean curvature *and* whether the motion is locally inward or outward. At the caps, H is positive but the motion is inward; conversely at the neck H is negative, at least for low values of λ, but the motion is outward.

A second interpretation for $\dot{a}$ is as the generator of a conformal mapping between nearby surfaces $\mathbf{X}(t) \to \mathbf{X}(t+\delta t)$. A packing on any surface in the family can be conformally mapped onto any other surface by transporting the particles along the normal trajectories and scaling them at each step according to $r \to r\sqrt{1+(\dot{a}/a)\,\delta t}$. In Fig. 2B and C, we use this property to map an arrested packing at $\lambda = 0.6$ onto a spherical surface $\lambda = 1$.

Considering coalescence scenarios with varying Γ, we expect for $\Gamma \ll 1$ to recover the static results as diffusion can fully relax the structure. Conversely, as $\Gamma \geq 1$, we expect that the history of compression and expansion will become imprinted upon the structure. To test this, we employ two different algorithms fully described in section 6 below. Static packings are produced on shapes of fixed λ using a Monte Carlo inflation algorithm inspired by the Lubachevsky–Stillinger algorithm[37]; we supplement this algorithm to ensure rigidity of the final packings and analyze the packings in Section 3. A second algorithm, which reproduces the scenario described above with particles diffusing on the evolving surface, is used to create arrested structures as a function of Γ which are analyzed in Section 4.

3 Statics

We first establish the role of the nonuniform geometry on the final states observed in arrested coalescence in the purely static case, where the particles are packed onto the surface so as to maximise the packing fraction ϕ. Using the protocol described in Methods, we generate $N = 100$ rigid packings each for surfaces with $\lambda \in [0.3, 1]$ and determine the neighbour graphs from the Delaunay triangulation. Representative packings are shown in Fig. 3A, where the particles are colored by coordination number c_i computed from the neighbour graph. Visually, and also from inspection of the density-density pair correlation function $g(s)$[38] (Fig. S3), these packings appear largely crystalline with the expected scars distributed over the whole surface.

The changing morphology is expected to have a number of effects from prior work. As the surface evolves from a bisphere at $\lambda = 0$ to a single sphere at $\lambda = 1$ at constant volume, the ratio r/R, where r is the particle radius and R the local radius of curvature at the cap, should decrease by a factor of $2^{1/3}$. The reduced influence of curvature is known to produce longer scars[6]. To verify this, scars are individually identified following[39] by deleting all vertices with six-fold coordination from the neighbour graph, leaving a disjoint *defect subgraph* visualized below the corresponding packings in Fig. 3B. The majority of scars exhibit a linear morphology independent of λ, but the average length increases up to around $\lambda = 0.6$ as shown in Fig. 3C while the fraction of singletons decreases (Fig. 3C inset).

Additionally, strong negative Gaussian curvature at the neck for low λ is expected to induce dislocations in excess of those topologically required. We follow[40] in defining the excess number of dislocations,

$$n_d = \frac{1}{2}\left(\frac{\sum_i |q_i|}{12} - 1\right), \tag{8}$$

where the sum is over particles and $q_i = c_i - 6$ is the dislocation charge of the ith particle, and display $n_d(\lambda)$ in Fig. 3D. As λ increases, the neck region becomes flatter and n_d decreases with a minimum at $\lambda = 0.6$. Above this value, more dislocations emerge to accommodate the positive curvature. Variation in the packing fraction $\phi(\lambda)$, also shown in Fig. 3D, is due to the dislocations since ϕ and n_d closely follow inverted trends.

Since the shape away from the neck is spherical, changes in n_d with λ are due to the curvature distribution around the neck. To test this, spatially resolved plots of the bond orientational order parameter $\psi_6 = \langle \exp(i6\theta)\rangle$[41] are calculated as described in Methods and shown in Fig. 3E for several λ. As the neck evolves, these distributions exhibit a transition: for $\lambda = 0.3$, the region near the neck has lower ψ_6 than the region at the cap, with a local maximum at around $z/a = 0.2$, while for $\lambda = 0.6$ the neck has *enhanced* ψ_6, and a less ordered region away from the neck. As λ increases further, the amplitude of this variation is reduced and becomes spatially uniform for the spherical case $\lambda = 1$. Consistent with the relation between ϕ and n_d, plots of the defect number density (Fig. S4) closely resemble the inverted form of ψ_6. The mean value of ψ_6 around the neck is shown as a function of λ in the inset of Fig. 3E and mirrors the trend exhibited by the packing
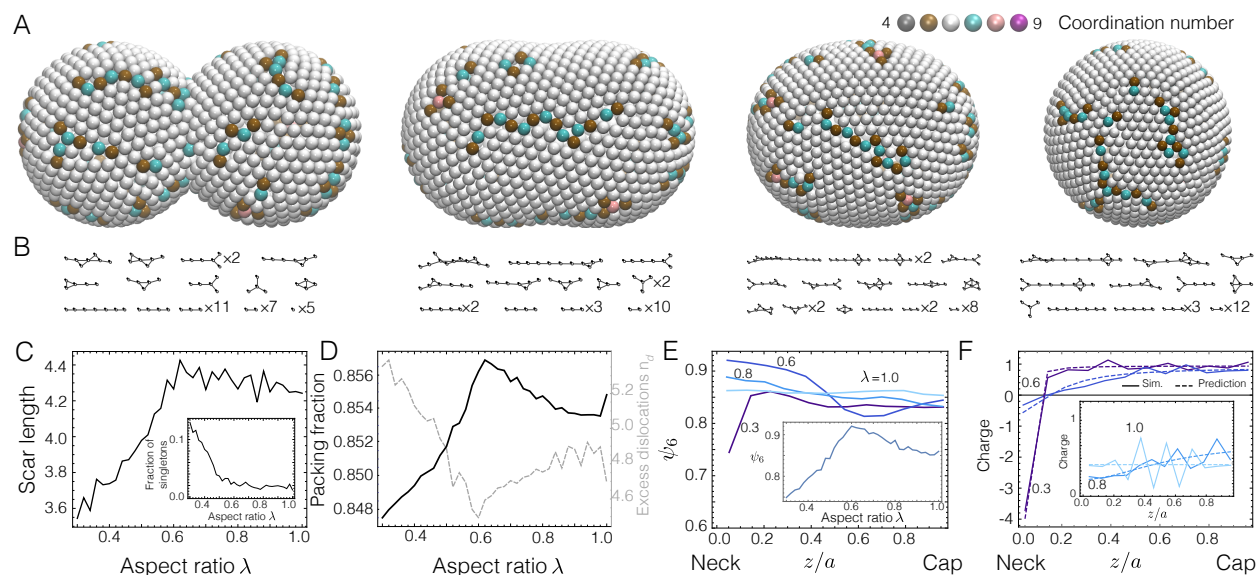
Fig. 3 Influence of static geometry on the microstructure. (A) Representative packing configurations for $\lambda = 0.3, 0.6, 0.8, 1.0$ and (B) their defect subgraphs. (C) Average scar length as a function of λ computed from defect subgraphs. *Inset:* Fraction of singletons as a function of λ. (D) Packing fraction ϕ (black) and excess dislocations n_d (grey) as a function of λ. (E) Bond orientational order parameter ψ_6 distribution along the rotational symmetry axis of the surface z/a. Inset shows the order parameter of the neck region for different stages of coalescence. (F) Charge distribution along the rotational symmetry axis of the surface z/a from packing (solid lines) and integrated Gaussian curvature (dashed lines) for $\lambda = 0.3, 0.6$ and (inset) $\lambda = 0.8, 1.0$.

fraction.

As shown in Fig. 3F and its inset, the defect charge density $\rho(z)$ (solid lines) can be well predicted from the integrated Gaussian curvature together with the topological constraint (dashed lines). These results explain the transition in the shape of $\psi_6(z)$ observed in Fig. 3E: For $\lambda = 0.3$, strongly negative Gaussian curvature at the neck tends to induce negative defects. Hence, additional positive charges must be generated at the ends to satisfy the topological constraint. Conversely, for $\lambda = 0.6$, fewer negative defects are induced and the neck region has almost zero Gaussian curvature leading to an overall enhancement of the order. Defects are needed outside the neck area to satisfy the charge constraint and also to match the positive curvature.

These results show that the role played by static geometry on the structures produced by arrested coalescence is generally consistent with the picture developed in the spherical crystallography literature[5]. Nonetheless, the family of surfaces studied here is unusual in that it incorporates regions of negative Gaussian curvature for some parameters but is also subject to the topological constraint imposed by constant Euler characteristic. This contrasts to studies on tori[14], where negative Gaussian curvature is always present, or on capillary bridges[15,29,42] where the Euler characteristic is not constant. The tension between the Gaussian curvature distribution and the topological constraint leads to interesting effects: For instance, the extremum in $\psi_6(\lambda)$, $\phi(\lambda)$ and $n_d(\lambda)$ occurs at $\lambda = 0.6$, where the neck is slightly negatively curved and *not* at $\lambda = 0.7$ where the Gaussian curvature at the neck becomes zero. Moreover, the fact that the neck can both diminish *and* enhance order depending on the particular distribution of K is surprising and could be further exploited as a means of controlling the local order in future work.

4 Kinetics

Having established the purely static role of the shapes, we are now equipped to untease the more subtle role of kinetics. To do so, a set of arrested states is generated using the protocol described in Methods, with $N = 800$ particles and suitable particle radius to promote a point of arrest λ_a for two different scenarios: an early arrest case with $\lambda_a \approx 0.3$, where the curvature of the neck is extremely negative and, as per Section 2 a strong compressive region exists close to the neck prior to arrest. The second case is where arrest occurs later at $\lambda_a \approx 0.6$, the point at which extrema in the packing fraction, defect density and bond orientational order were found to occur in the previous section; for this scenario particles at the neck are being pushed apart by the constraint forces. In both cases, compressive regions exist in both scenarios around the caps.

The ratio of diffusion time scale to the total relaxation time $\theta = \tau_d/\tau_r$ is varied from 2^{-8} to 2^4 to control the relaxation speed, with 50 samples for each value. The corresponding values of $\Gamma = |\dot{A}|/(ND)$ at the point of arrest, linearly related to θ as discussed in Section (2), is calculated for each simulation. Faster relaxation, as expected, generically leads to less ordered structures for both early and late arrest scenarios as shown in Fig. 4A where $\langle \psi_6 \rangle$ is displayed as a function of Γ. Overall the order is higher for late arrest which is consistent with the static results of Fig. 3E and is therefore geometric in origin. Faster relaxation also halts the arrest at a earlier point. For early arrest, λ_a decreases from 0.34 to 0.32 as θ increases from 2^{-8} to 2^4, with λ_a from 0.63 to 0.59 for late arrest.

A significant difference in the two scenarios emerges, however, when the spatially resolved order of the arrested states is exam-
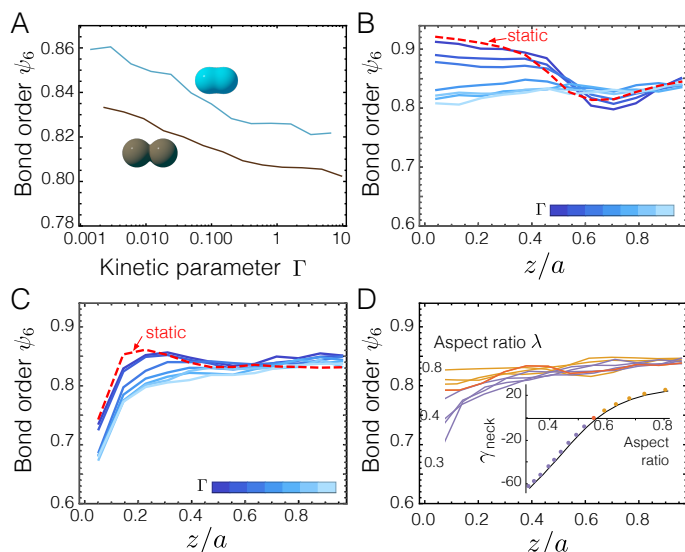
Fig. 4 Influence of kinetics on the microstructure. (A) Mean bond orientational order parameter ψ_6 of all particles as a function of Γ. Brown is for system arrested at $\lambda_a \approx 0.3$ and blue at $\lambda_a \approx 0.6$. (B) Bond orientational order parameter ψ_6 distribution along the surface for late arrest $\lambda_a \approx 0.6$ at different values of the kinetic parameter $\Gamma = (0.0028, 0.012, 0.048, 0.20, 0.39, 1.58, 6.36)$. The red dashed line is the distribution for static packing. (B) Corresponding plot for $\lambda_a \approx 0.3$ with $\Gamma = (0.0023, 0.0091, 0.037, 0.15, 0.59, 2.38, 9.5)$. (D) ψ_6 distribution as a function of the aspect ratio of the arrest point for fast relaxation $\Gamma \sim 10$. Inset: Local rate of area change per particle at the neck as a function of λ for fast relaxation.

ined. Shown in Fig. 4B and C is $\psi_6(z)$ for $\lambda_a \approx 0.6$ and $\lambda_a \approx 0.3$ respectively. Different traces correspond to different values of Γ and, as before, the left and right portions of the doublet are combined into one plot. In both cases, the static order parameter distribution, shown by the red dashed line, is recovered for sufficiently slow relaxation.

For late arrest, the quasistatic limit includes an enhancement of ψ_6 in the flatter central area and reduced order closer to the cap. As Γ increases, the distributions remain similar in shape but are reduced in amplitude and as $\Gamma > 1$, the orientational order converges on a uniform constant value of ≈ 0.83. In contrast, for late arrest the distribution of ψ_6 remains similar in form as a function of Γ: there is a strong reduction in the order parameter around the neck and a uniform distribution near the cap. Increasing Γ reduces the order globally, shifting the curves down by as much as 0.1 but does not change their overall form.

To characterize this transition more carefully, a new ensemble of simulations with different arrest points λ_a is run in the kinetically dominated regime $\Gamma \approx 10$ and the resulting distributions of ψ_6 are shown in Fig. 4D. Comparing these with equivalent plots for static packings in Fig. 3E, we see that for arrest earlier than $\lambda \sim 0.5$, the static and dynamic order distributions appear similar, although the overall values of ψ_6 are reduced, shown as purple curves. The signature of the geometry therefore remains imprinted on the microstructure independently of Γ. For arrest after $\lambda \sim 0.5$, the distributions no longer resemble the static distributions, having approximately uniform $\psi_6 \approx 0.83$, shown as yellow

curves. Rapid relaxation therefore appears more readily able to wash out variations caused by the nonuniform curvature for late arrest. The boundary of the two regimes at $\lambda_a = 0.55$ is displayed as the red curve and is entirely different from the static distribution, incorporating two minima. The transition coincides with the point at which the neck ceases to promote compression as shown in the inset of Fig. 4D where γ at the point of arrest is plotted as a function of λ.

Time-resolved analysis

Time resolved analysis of the microstructure in the kinetically dominated regime $\Gamma \gg 1$ allows us to probe the transition further. The particle number density is plotted at several time points t/t_f in Fig. 5A for the late arrest scenario $\lambda_a \approx 0.6$, together with plots of the ψ_6 distribution calculated as described in Methods in Fig. 5B and snapshots of the configuration in Fig. 5E. Here t_f is defined to be the time at which arrest occurs. Corresponding plots and visualizations for early arrest $\lambda_a \approx 0.3$ are displayed in Fig. 5C, D and F respectively. Movies corresponding to Fig. 5E and F are supplied as Supplementary Material.

These plots reveal how the history of expansion and compression predicted in Section (2) causes the evolution in order. Fig. 1E shows the area change profiles across the surfaces with different aspect ratios. The cap area is compressed during the evolution of surfaces while the neck area initially is compressed and then expanded.

For the late arrest scenario, particles are initially uniformly ordered, except close to the neck. As relaxation proceeds, compression at the cap produces a denser region that converges to $\psi_6 \sim 0.83$, reminiscent of the jamming fronts observed in [22]. This value is similar to the order at the cap in static packings. At the neck, the particles are initially *less* ordered because of the strong concentration of negative Gaussian curvature, and the initial compressive region that increases the local density begins to widen the disordered region. As λ passes 0.4, however, the widening stops, and as λ increases further the ordered region growing in from the caps completely overcomes the disordered neck region, yielding the final state uniform in density and ψ_6.

For the early arrest scenario, order at the cap changes very little through the course of the simulation, remaining similar to the static value. The initially disordered region at the neck begins to widen, as it does for the late arrest scenario, and reaches a maximum width at around $\lambda = 0.25$. After this, the neck region begins to uniformize but does not completely do so, freezing in the disordered region that is also seen in the static case.

The influence of kinetics on the microstructure therefore depends critically on the arrest point: the history of compression and expansion of the surface, quantified by γ, can freeze in disordered regions caused by the underlying curvature even where kinetics might be expected to wash out the effect of geometry. For early arrest, the strong initial compression leads to a disordered region that is frozen in at all relaxation speeds tested, while for late arrest fast relaxation fully blurs out the nonuniform distribution of order promoted by geometry. The evidence of this section suggests that, at least crudely, it is the form of γ immediately prior
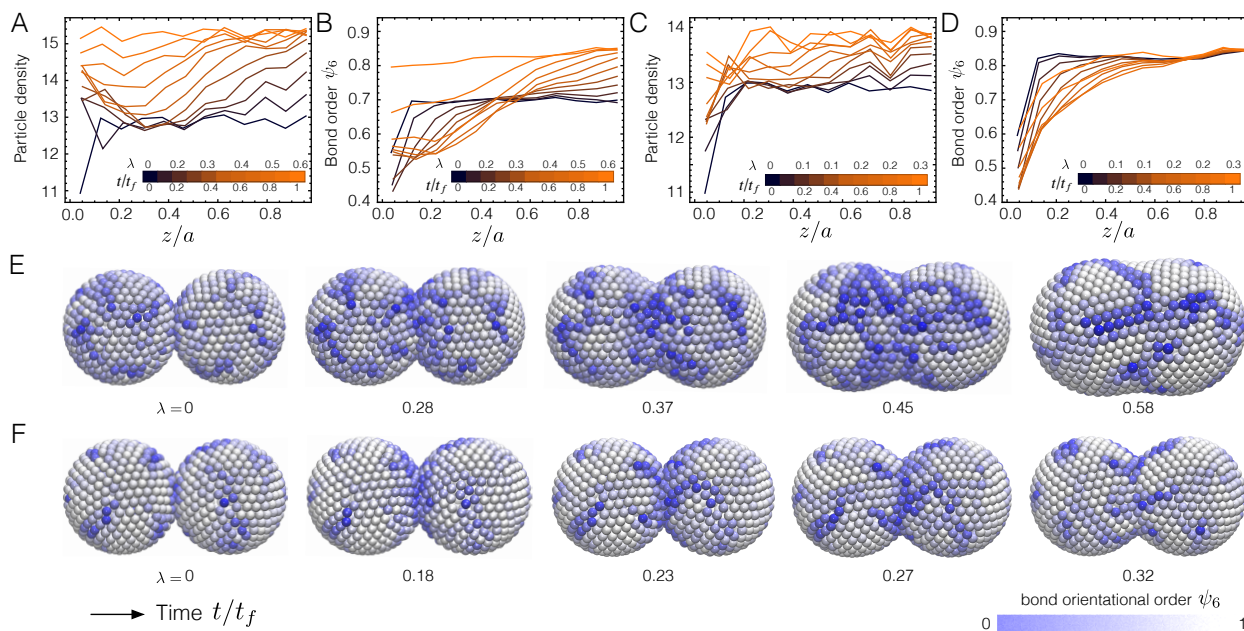
Fig. 5 Time resolved evolution of the microstructure for the kinetically dominated regime. Distributions of (A) particle number density and (B) bond orientational order parameter ψ_6 as a function of time for late arrest $\lambda_a \approx 0.6$ and fast relaxation $\Gamma = 9.5$. (C) and (D) Corresponding plots for early arrest $\lambda_a \approx 0.3$. (E) and (F) Representative visualizations for $\lambda_a \approx 0.6$ and $\lambda_a \approx 0.3$ respectively; particles are colored by ψ_6.

to arrest that is most important for determining the microstructure: for example, the late arrest scenario $\lambda_a \sim 0.6$, the compressive regions that exist early in the relaxation appear to have little influence on the final state.

Non-Affine Response

The picture developed thus far is of the response of the particles to local expansion or compression induced by the evolving surface, but this neglects other kinds of deformation that may be present. Consider a group of particles with initial coordinates $\mathbf{x}_i(\lambda)$ that all lie in some probe ball $|\mathbf{x}_i - \mathbf{x}_0| < \rho$ and are transported from $\mathbf{x}_i(\lambda) \to \mathbf{x}'_i(\lambda + \delta\lambda)$ consistent with Eq. (1). Their final location is determined both by the moving surface constraints, which locally induce scale and shear deformations as illustrated in Fig. 2, as well as interaction with other particles. This very complex environment can potentially induce non-affine deformations of the local particle configuration. To resolve these, we use the quantity D^2_{min} as constructed by Falk and Langer[19],

$$D^2_{min} = \min \sum_j \left[\Delta x_j(\lambda) - E \cdot \Delta \mathbf{x}_j(\lambda + \delta\lambda) \right]^2, \qquad (9)$$

where $\Delta x_j(\lambda) = x_j(\lambda) - x_0(\lambda)$ is the displacement of the jth particle from a reference particle on the surface λ, E is a strain tensor, and D^2_{min} is to be minimized with respect to the components of E. Hence, D^2_{min} is a measure of the residual motion of the particles that cannot be explained by the affine deformation E closest in a least-squares sense.

In Fig. 6B, we show the mean D^2_{min} per particle as a function of simulation time for a late arrest $\lambda_a \approx 0.6$ simulation; spatially resolved plots at different time points are shown in Fig. 6A. Non-affine deformation is significant both early in the evolution and

as the arrest point is approached; it is always localized to varying degrees in the neck. For early times, large D^2_{min} is due to the strong curvature of the neck where transport of the particles along the normal by the surface constraint induces non-affine motion. Conversely, approaching the arrest point the solidification fronts growing from either end as identified above (Fig. 5) must meet in the middle. Here, interparticle interactions are primarily responsible for the non-affine motion as the curvature at the neck is rather weak.

Spatially resolved analysis of D^2_{min} reveals a complex picture and considerable caution must be used in interpreting these events. Tantalizingly, however, we do see spatially localized plastic deformations reminiscent of the Shear Transition Zones that govern the plastic response of amorphous metallic glasses and were the original reason D^2_{min} was introduced[19–21]. In Fig. 6C-F we show two events, each with a sequence of snapshots of particle configurations close to the arrest point displaying particle configurations colored by D^2_{min} and ψ_6. The first event, depicted in Fig. 6C&D, more closely resembles an STZ in that it is a spatially localized and evanescent region with large D^2_{min} and little visible nearby rearrangement. The second, shown in Fig. 6E&F, is a plastic rearragement that leads to the formation of a dislocation. It is accompanied by spatially extended lineslips revealed in ψ_6 and hence is *not* an STZ. We see many similar events of both types, and events with large D^2_{min} occur for all local values of ψ_6 defying a simple categorization. A systematic analysis of the non-affine response and its interaction with the spatially evolving manifold therefore remains for future work.

5 Conclusion

This work has demonstrated a rich interplay between geometry and kinetics in determining the structure of arrested coalescence
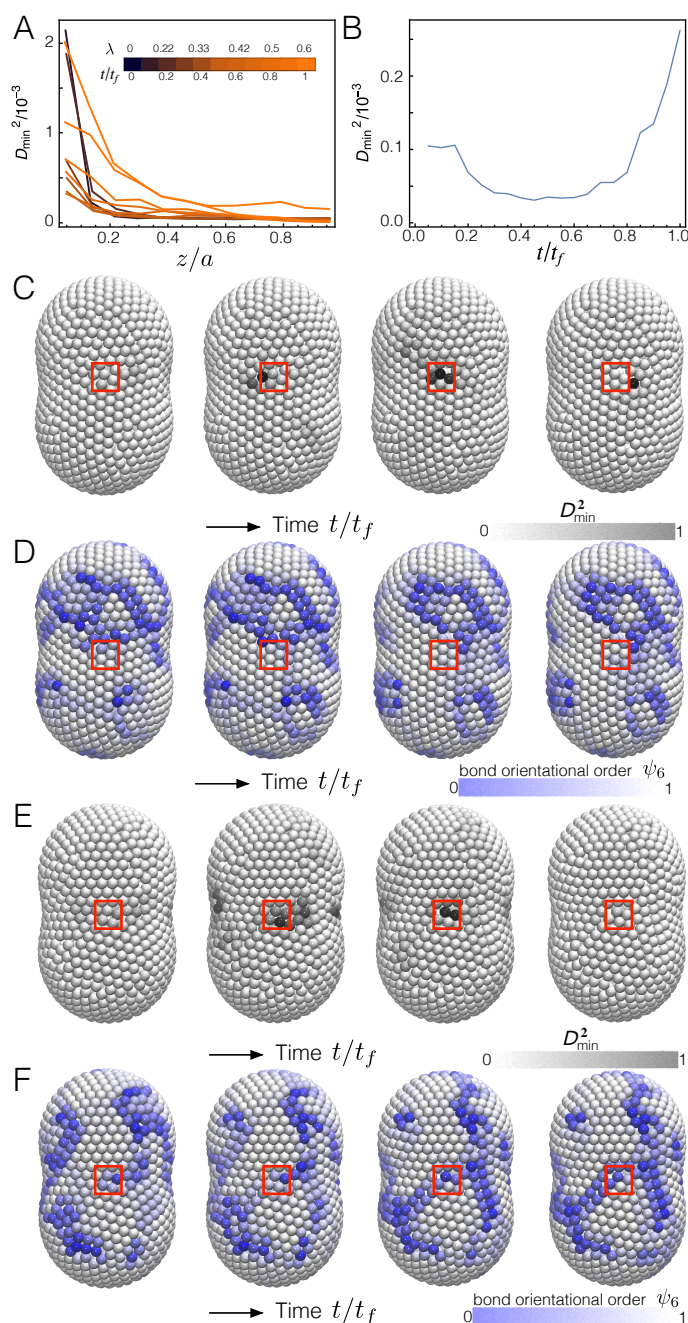
Fig. 6 Non-affine motion of the particles. D^2_{min}, the deviation from affine deformation, of late arrest $\lambda_a \approx 0.6$ for kinetically dominated regime. (A) D^2_{min} distribution along the rotational symmetry axis of the surface z/a at different time t/t_f. (B) Average D^2_{min} as a funtion of time t/t_f. (C-D) and (E-F) Two events with large spatially localized D^2_{min}. For each event, a time resolved sequence of configurations is shown with particles colored by D^2_{min}, scaled to the maximum value ocurring in the sequence (C&E) and, separately the bond orientational order parameter ψ_6 (D&F). Red boxes indicate the region of interest discussed in the main text.

droplets. In contrast to other kinds of colloidosomes, such as spheres, the dramatic shape changes and strong curvatures that occur here lead to interesting effects. While the static influence on the structure was found to be well predicted by the integrated Gaussian curvature together with the topological requirement on the defect charge, the shapes produced by arrested coalescence form an unusual example of a system both with variable amounts of negative Gaussian curvature and a topological constraint. The role of kinetics is quantified by the parameter $\Gamma = \dot{A}/(ND)$ the ratio of the rate of change of area per particle to its diffusion constant. As $\Gamma \to 0$, the microstructure closely resembles the static packing scenario where the system distributes defects to match the Gaussian curvature.

At finite Γ, kinetics tends to blur out variation in the order as the structure can no longer be fully relaxed. Disordered regions can nonetheless remain because, as the surface relaxes, local regions of compression induce solidification that can trap them, hence retaining a memory of the evolution. The growing solid regions resemble dynamic jamming fronts observed under impact and shear of dense suspensions of colloidal particles, but here are induced by the locally changing metric of the surface rather than by an external influence. Prediction of the local compression rate from differential geometry of the surface, Eq. (6), shows that kinetic influences depend on geometric quantities such as the mean curvature that are extrinsic in origin, i.e. depending on the embedding. Moreover, significant non-affine deformations occur both due to the complex geometry of these systems and the solidification fronts growing from the caps. Some of these resemble Shear Transition Zones observed in amorphous materials [19–21], but many others do not and a complete understanding of the non-affine response remains to be developed.

Arrested colloidosomes, which possess a natural parameter Γ that quantifies the degree of nonequilibrium behavior and "remember" the evolution of the shapes that produced them, may serve as a model system for exploring memory formation in matter [26]. The remarkably rich influence of kinetics also suggests the possibility of exploiting it as a means to control the microstructure of colloidosomes. One can imagine designing a shape using Eq. (6) that incorporates compressive regions prior to arrest and selectively locks in disordered regions that become targets for further coalescence events in multistage assembly. The extent of the design space for this remains unknown, however: The Young-Laplace equation Eq. (7) implies that the mean curvature and the local normal velocity are not independent, but that they differ here is because of the overall volume constraint.

A final direction to be pursued is the connection of these arrested shapes to *jamming*, a transition to rigidity as a function of density that occurs in particulate media [43,44]. While the kinetically arrested structures observed here are *not* jammed, in that they may possess unconstrained collective motions of particles, the static packings we use as a comparison *are* because this is explicitly enforced. Two of the present authors recently proposed that rigid structures formed as a result of shape evolution form a new class called *"metric jamming"* [18] where the final state is rigid both with respect to perturbations of the particles and the manifold on which they are embedded. Analysis of the arrested

coalescence problem along these lines may help determine the longevity of the undoubtedly metastable arrested structures, as well as provide tools to determine their mechanical properties.

6 Methods

Static packings—Particles are initially dispersed with their center of mass on the surface at zero radius, diffused by Brownian motion according to the Langevin equation,

$$\mathbf{x}_i^{'}(t + \Delta t_p) = \mathbf{x}_i(t) + \eta_i\sqrt{2D\Delta t_p}, \tag{10}$$

where η_i is a random step drawn from Gaussian distribution along the tangent plane, and D is the diffusion constant such that the variance of stepsize for Brownian motion in time t is $2Dt$. We may therefore define a characteristic diffusion time scale τ_d that gives a standard deviation of stepsize equal to the particle diameter,

$$2r = \sqrt{2D\tau_d}. \tag{11}$$

As the particles diffuse, their radii r are increased (inflation moves) very slowly, with $\frac{\delta r}{\sqrt{2Dt}} \sim 10^{-4}$ in unit time. Collective motions that undo overlap are found at each stage by gradient descent on an artificial potential,

$$V_{overlap} = \begin{cases} r^2 - rx & x < r \\ 0 & x \ge r \end{cases}, \tag{12}$$

that penalizes overlap. The simulation is halted when no further move is possible without inducing overlaps.

Generically, packings produced by this algorithm need not be rigid, i.e. there may exist collective motions of particles that can unjam the system and allow further relaxation of the surface. We therefore adapt [18] a linear programming approach [45] to identify these collective motions, execute them, and restart the packing simulation. Before applying the linear program, the configuration is conditioned by minimizing an artificial soft repulsive potential imposed between all pairs of particles; this tends to push the particles away from one another. This process is repeated until a rigid final state is achieved.

Dynamic simulations—A second algorithm was used to understand how the relaxation process affects the final structure. For these simulations, particles are initially dispersed by random sequential deposition with a fixed particle radius r on the surface of $\lambda = 0$. During the simulation, diffusion moves are made as before in Eq. (10). During relaxation moves, the particles are constrained to the surface with overlaps prevented to first order using Lagrange multipliers [46]. After each relaxation step, Eq. (12) is minimized to remove overlaps. If not all overlaps could be undone, the timestep is reduced. The algorithm halts when the timestep of relaxation is smaller than a threshold δt.

Order parameter calculation—Spatially resolved plots of the bond orientational order parameter $\psi_6 = \langle \exp(i6\theta) \rangle$ [41] (the average is taken from neighbor particles) are calculated by first, projecting each particle and its neighbors to the tangent plane of the center particle to calculate the order ψ_6^i for that particle. The surface is then divided into 24 equal-area axially symmetric regions and the symmetry of the shape is exploited by collapsing corresponding regions for positive and negative z; the mean ψ_6 is computed for all particles in each region.

For kinetic simulations, neighbors of particles are not determined from Delaunay triangulation since the particles are generally not densely packed during the coalescence. Instead, we define neighbors as particles within the center-to-center distance of 1.5 times diameter. In practice, this definition changes the numerical values of ψ_6 very little and doesn't change the trend of evolution.

References

1 A. B. Pawar, M. Caggioni, R. Ergun, R. W. Hartel and P. T. Spicer, *Soft Matter*, 2011, **7**, 7710–7716.

2 A. R. Studart, H. C. Shum and D. A. Weitz, *The Journal of Physical Chemistry B*, 2009, **113**, 3914–3919.

3 G. Dockx, S. Geisel, D. G. Moore, E. Koos, A. R. Studart and J. Vermant, *Nature Communications*, 2018, 1–8.

4 A. B. Pawar, M. Caggioni, R. W. Hartel and P. T. Spicer, *Faraday discussions*, 2012, **158**, 341–350.

5 M. J. Bowick and L. Giomi, *Advances in Physics*, 2009, **58**, 449–563.

6 A. Bausch, M. Bowick, A. Cacciuto, A. Dinsmore, M. Hsu, D. Nelson, M. Nikolaides, A. Travesset and D. Weitz, *Science*, 2003, **299**, 1716–1718.

7 H. Seung and D. R. Nelson, *Physical Review A*, 1988, **38**, 1005.

8 A. Pérez-Garrido, M. Dodgson and M. Moore, *Physical Review B*, 1997, **56**, 3640.

9 M. J. Bowick, D. R. Nelson and A. Travesset, *Physical Review B*, 2000, **62**, 8738.

10 M. Bowick, A. Cacciuto, D. R. Nelson and A. Travesset, *Physical Review Letters*, 2002, **89**, 185502.

11 M. J. Bowick, A. Cacciuto, D. R. Nelson and A. Travesset, *Physical Review B*, 2006, **73**, 024115.

12 V. Vitelli, J. B. Lucks and D. R. Nelson, *Proceedings of the National Academy of Sciences*, 2006, **103**, 12323–12328.

13 L. Giomi and M. Bowick, *Physical Review B*, 2007, **76**, 054106.

14 L. Giomi and M. J. Bowick, *Physical Review E*, 2008, **78**, 010601.

15 W. T. Irvine, V. Vitelli and P. M. Chaikin, *Nature*, 2010, **468**, 947–951.

16 M. Brojan, D. Terwagne, R. Lagrange and P. M. Reis, *Proceedings of the National Academy of Sciences*, 2015, **112**, 14–19.

17 F. L. Jiménez, N. Stoop, R. Lagrange, J. Dunkel and P. M. Reis, *Physical review letters*, 2016, **116**, 104301.

18 C. J. Burke and T. J. Atherton, *arXiv preprint arXiv:1605.09478*, 2016.

19 M. L. Falk and J. S. Langer, *Physical Review E*, 1998, **57**, 7192.

20 J. Langer, *Scripta materialia*, 2006, **54**, 375–379.

21 M. L. Falk and J. S. Langer, *Annu. Rev. Condens. Matter Phys.*, 2011, **2**, 353–373.

22 S. R. Waitukaitis and H. M. Jaeger, *Nature*, 2012, **487**, 205.

23 I. R. Peters, S. Majumdar and H. M. Jaeger, *Nature*, 2016, **532**, 214.

24 E. Han, I. R. Peters and H. M. Jaeger, *Nature communications*, 2016, **7**, 12243.

25 S. Majumdar, I. R. Peters, E. Han and H. M. Jaeger, *Physical Review E*, 2017, **95**, 012603.

26 N. C. Keim, J. D. Paulsen, Z. Zeravcic, S. Sastry and S. R. Nagel, *Rev. Mod. Phys.*, 2019, **91**, 035002.

27 E. Vignati, R. Piazza and T. P. Lockhart, *Langmuir*, 2003, **19**, 6650–6656.

28 R. S. Garabedian and J. J. Helble, *Journal of colloid and interface science*, 2001, **234**, 248–260.

29 H. Kusumaatmaja and D. J. Wales, *Physical review letters*, 2013, **110**, 165502.

30 N. A. García, A. D. Pezzutti, R. A. Register, D. A. Vega and L. R. Gómez, *Soft Matter*, 2015, **11**, 898–907.

31 N. A. García, R. A. Register, D. A. Vega and L. R. Gómez, *Physical Review E*, 2013, **88**, 012306.

32 L. R. Gómez, N. A. García, V. Vitelli, J. Lorenzana and D. A. Vega, *Nature communications*, 2015, **6**, 6856.

33 G. Meng, J. Paulose, D. R. Nelson and V. N. Manoharan, *Science*, 2014, **343**, 634–637.

34 J. Eggers, J. R. Lister and H. A. Stone, *Journal of Fluid Mechanics*, 1999, **401**, 293–310.

35 A. Menchaca-Rocha, A. Martinez-Davalos, R. Nunez, S. Popinet and S. Zaleski, *Physical Review E*, 2001, **63**, 046309.

36 M. Wu, T. Cubaud and C.-M. Ho, *Physics of Fluids*, 2004, **16**, L51–L54.

37 B. D. Lubachevsky and F. H. Stillinger, *Journal of Statistical Physics*, 1990, **60**, 561–583.

38 A. Donev, S. Torquato and F. H. Stillinger, *Physical Review E*, 2005, **71**, 011105.

39 A. M. Mascioli, C. J. Burke, M. Q. Giso and T. J. Atherton, *Soft Matter*, 2017, **13**, 7090–7097.

40 C. J. Burke, B. L. Mbanga, Z. Wei, P. T. Spicer and T. J. Atherton, *Soft Matter*, 2015, **11**, 5872–5882.

41 D. R. Nelson and B. Halperin, *Physical Review B*, 1979, **19**, 2457.

42 W. T. Irvine and V. Vitelli, *Soft Matter*, 2012, **8**, 10123–10129.

43 S. Torquato and F. H. Stillinger, *Reviews of modern physics*, 2010, **82**, 2633.

44 A. J. Liu and S. R. Nagel, *Annu. Rev. Condens. Matter Phys.*, 2010, **1**, 347–369.

45 A. Donev, S. Torquato, F. H. Stillinger and R. Connelly, *Journal of Computational Physics*, 2004, **197**, 139–166.

46 F. J. Vesely, *American Journal of Physics*, 2013, **81**, 537–544.

We disentangle the influence of shape and kinetics in the structure of arrested Pickering emulsion droplets after coalescence.